The Tensile Response and Fracture Behavior of an Al-Zn-Mg-Cu Alloy: Influence of Temperature

T.S. Srivatsan, S. Anand, D. Veeraghavan, and V.K. Vasudevan

A high-performance, high-strength, and novel Al-Zn-Mg-Cu alloy in the T7751 condition was deformed to failure in laboratory air environment at ambient and elevated temperatures. Temperature influenced the tensile response of the alloy for both the longitudinal and transverse orientations. Strength decreased with an increase in test temperature, with a concomitant improvement in ductility. Test results indicate the alloy response to be the same for both the longitudinal and transverse orientations. No major change in the macroscopic fracture mode was observed with the direction of testing. Tensile fracture, on a microscopic scale, revealed features reminiscent of both ductile and brittle mechanisms. The microscopic fracture behavior was a function of test temperature. The mechanisms and intrinsic micromechanisms governing the tensile fracture process are discussed in terms of mutually interactive influences of microstructural effects, matrix deformation characteristics, test temperature, and grain boundary failure.

Keywords
aluminum alloy, deformation, fracture, microstructure

1. Introduction

THE SUSTAINED requirement for new and improved materials for a spectrum of high-performance applications in the aerospace and ground transportation industries is driven by a fascinating mix of scientific, economical, and even military motivations. These materials, while offering considerable savings in weight, must concurrently be durable and damage tolerant for a wide variety of applications ranging from airframe structures for aircraft to space vehicles, including lightweight armored carriers. In fact, the sustained success achieved with high-strength aluminum alloys coupled with the tried and true design concept, aided by a consistent record of continuous improvement in alloy development efforts and cost effectiveness, has provided resistance to the adoption of alternative materials. The stringent demands placed on the newer generation of military and civilian aircraft has engendered considerable scientific and technological interest in the development, emergence, and use of new and improved aluminum alloys as attractive and viable alternatives to the existing high-strength commercial alloys belonging to the 2*xxx* and 7*xxx* series. However, extensive use of age-hardenable 2*xxx*-series and 7*xxx*-series alloys, at high strength levels, was hampered by their poor secondary properties of toughness, stress corrosion cracking, and cyclic fatigue resistance, particularly in the short transverse direction.

The intrinsic ability to predict and control microstructures was established as the most viable and attractive technique to achieve notable improvements in toughness, stress corrosion resistance, cyclic fatigue resistance, and fracture properties (Ref 1). Microstructural control can be systematically achieved through changes in alloy chemistry (Ref 2-5), the use of grain refining elements (Ref 4-6), minimizing the level of the impurity elements (Ref 6, 7), and the use of novel thermomechanical processing treatments (Ref 8-14), which result in the emergence of derivative alloys and tempers.

A series of alloy development efforts, achieved strictly through compositional modifications, resulted in the development and emergence of aluminum alloy 7055 (Ref 14). The development and use of the T7*x*-type temper for the Al-Zn-Mg-Cu-series alloys solved many of the problems associated with stress corrosion cracking and exfoliation corrosion (Ref 14, 15). One such temper developed at the Aluminum Company of America (ALCOA) is T77, which offered the possibility of enhancing corrosion resistance without sacrificing strength. The attractive properties of alloy 7055-T77 were attributed to its high ratio of zinc to magnesium and copper to magnesium (Ref 14). The composition provides a microstructure at and near the grain boundaries that is resistant to both intergranular fracture and corrosion.

The objective of this study is to establish the influence of temperature on tensile response and fracture characteristics of aluminum alloy 7055-T7751. Accordingly, to understand the influence of elevated temperatures on the macroscopic fracture mode and microscopic mechanisms governing fracture, the fracture behavior of the alloy was evaluated at elevated temperatures and compared with the fracture characteristics at ambient temperature. The kinetics governing the tensile fracture behavior of the alloy were examined in light of mutually interactive influences of test temperature, intrinsic microstructural effects, matrix deformation characteristics, and the micromechanisms that promote failure.

2. Material

The 7055 aluminum alloy used in this experimental investigation was provided by ALCOA as 25-mm-thick extruded plate in the T7751 condition. Table 1 shows the nominal chemical composition (in weight percent) of the alloy. This alloy is a modified version of alloy 7150 with lower levels of the impurity elements iron and silicon. Zirconium present in the alloy controls the grain size and suppresses recrystallization. It combines with aluminum to form the metastable Al_3Zr phase (β') that precipitates during the ingot preheat and homogenization

T.S. Srivatsan and **S. Anand,** University of Akron, Akron, OH 44325-3903, USA; **D. Veeraghavan** and **V.K. Vasudevan,** University of Cincinnati, Cincinnati, OH 45221-0012, USA.

treatment. These particles, referred to as dispersoids, are insoluble intermetallic compounds that play an important role in controlling the deformation and fracture process (Ref 4, 16-18). The T7751 temper designation refers to a proprietary thermomechanical treatment that involves solution heat treatment, water quench, and a permanent stretch prior to artificial aging. The higher solute (copper) content, compared to alloy 7150, accounts for superior strength during aging, increasing the temperature range of Guinier-Preston zone stability and enhanced resistance to corrosion (Ref 19).

3. Experimental Techniques

Cylindrical test specimens, conforming to specifications in ASTM:E8-93 (Ref 20), were precision machined from the as-received 7055-T7751 plate. The stress axes of the specimens were parallel (longitudinal) and perpendicular (transverse) to the rolling direction. The test specimens measured 25 mm in length by 6.25 mm in diameter. To minimize the effects of surface irregularities, final surface preparation was achieved by mechanically polishing the gage sections using 600-grit emery paper finish polished to remove any and all circumferential scratches and surface machining marks.

Uniaxial tensile tests were performed up to failure on a fully automated, closed-loop, servohydraulic mechanical test machine (Instron Corporation, Canton, MA) equipped with a 100 kN load cell. The specimens were deformed at a constant strain rate of $10^{-4}\,s^{-1}$. The tests were performed in controlled laboratory air environment (relative humidity = 55%) at ambient (27 °C) and elevated temperatures (100 and 190 °C). The highest test temperature corresponds to the temperature at which the alloy was artificially aged. The elevated temperature tests were conducted using an INSTRON (INSTRON Corporation, Canton, MA) environmental chamber. The temperature was controlled with the aid of a temperature controller fixed on the surface of the specimen. Maximum temperature variation was well within 2 °C of the set-point temperature over the entire duration of the test. Ambient temperature varied from 27 to 29 °C during any given test. Before each test, the specimen was maintained or soaked at the test temperature for 30 min to achieve stability with the environment. The axial strain was measured using a 12.7 mm clip-on extensometer fixed, using rubber bands for room temperature tests and steel springs for the ele-

Table 1 Nominal chemical composition of aluminum alloy 7055-T7751, 1.048 in. thick rolled plate

Element	Composition, wt%
Cu	2.41
Mg	2.00
Zn	8.21
Zr	0.11
Mn	0.005
Cr	0.003
Al	Balance

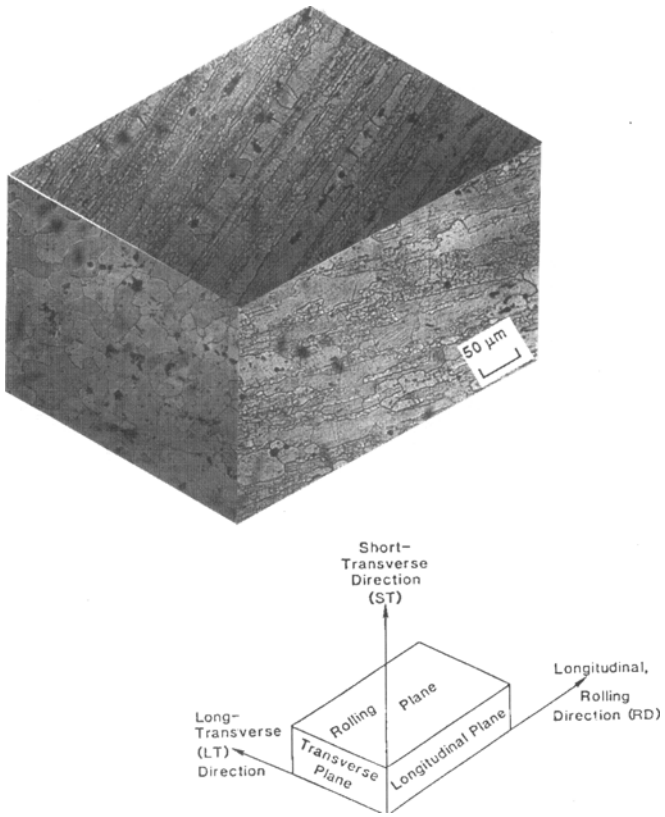

Fig. 1 Triplanar optical micrograph illustrating the grain morphology of aluminum alloy 7055

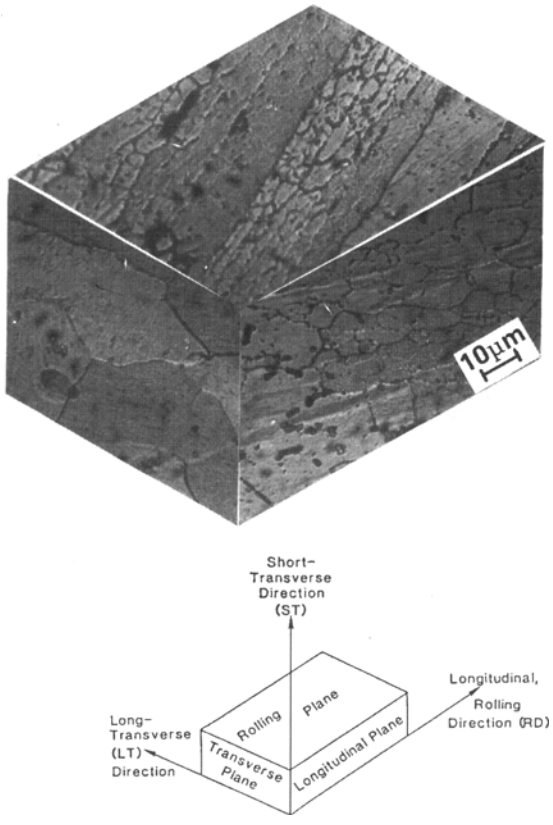

Fig. 2 Triplanar optical micrograph illustrating constituent particle density and distribution along the three orthogonal directions of the wrought plate

vated temperature tests, to the specimen gage section. The stress and strain measurements, parallel to the load line, were recorded on a personal computer based data acquisition system.

Metallographic samples were cut from the three orthogonal directions of the as-received plate. The samples were mounted in bakelite and wet ground on 320-, 400-, and 600-grit silicon carbide paper using water as a lubricant. Subsequently, the ground samples were mechanically polished using one micron alumina-based polishing compound. The polished samples were etched with Keller's reagent, examined in an optical microscope, and photographed using a standard bright-field illumination technique to reveal the grain boundaries and overall grain morphology.

Fracture surfaces of the fully deformed tensile samples were examined in a scanning electron microscope (SEM) to determine the macroscopic fracture mode and characterize the fine-scale topography and microscopic mechanisms governing quasi-static fracture. The distinction between the macroscopic mode and microscopic fracture mechanism is based on the magnification level at which the observations are made. The macroscopic mode refers to the nature of failure, while the microscopic mechanism relates to the local failure process (microvoid formation, coalescence, and nature of cracking). Samples for SEM observation were obtained from the deformed tensile specimens by sectioning parallel to the fracture surface.

4. Results

4.1 *As-Received Microstructure*

The microstructure of the as-received 7055 alloy is shown in Fig. 1 and 2 as triplanar optical micrographs illustrating the grain structure and constituent particle distribution in the three orthogonal directions of the wrought plate. The microstructure was partially recrystallized with fairly large recrystallized grains that were flattened and elongated parallel to the longitudinal (rolling) direction, as a direct consequence of the deformation introduced by the rolling operation. The unrecrystallized regions are comprised of both subgrains (with low-angle grain boundaries) and very fine recrystallized grains (with high-angle grain boundaries). Because of the very fine nature of this mixed structure, coupled with the difficulty in distinguishing

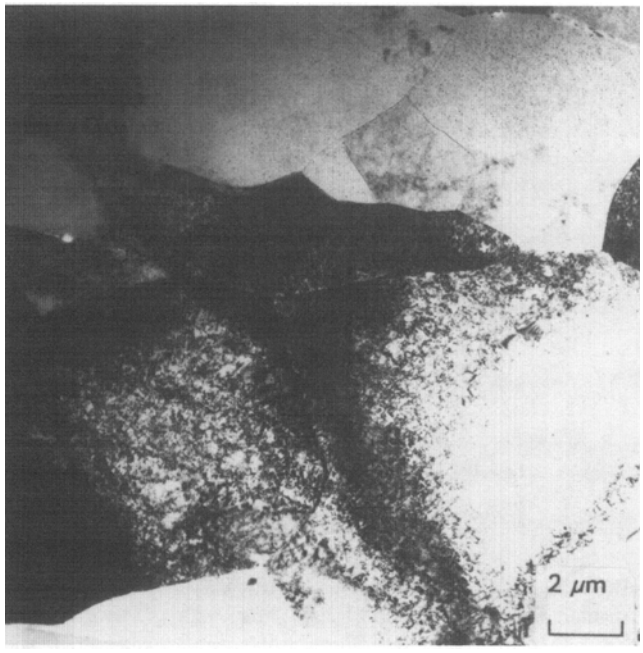

Fig. 3 Bright field TEM showing well-defined grains of nonuniform size in the recrystallized region

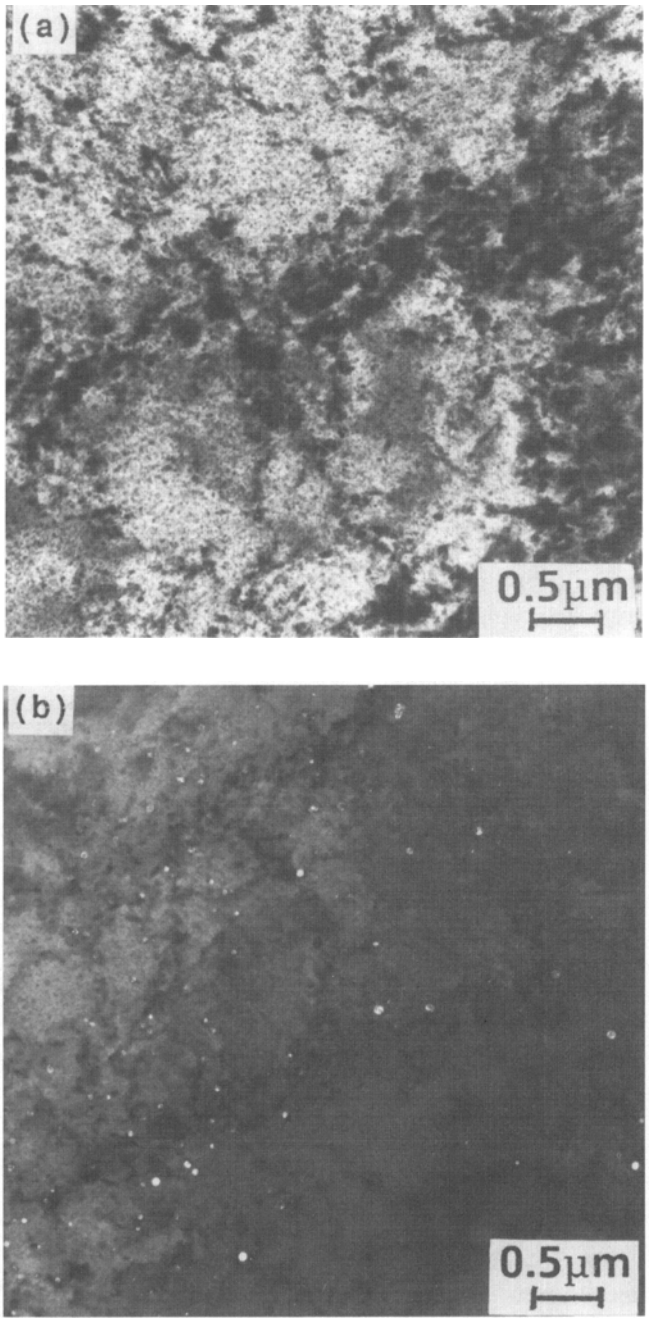

Fig. 4 Transmission electron micrographs showing the intermediate η′ precipitates dispersed in the alloy matrix. (a) Bright field. (b) Dark field

between these two components, entire regions of this nature are designated as being "unrecrystallized." The recrystallized grain size was nonuniform along each of the three orthogonal directions of the wrought plate, resulting in an anisotropic microstructure. At higher magnifications, the insoluble iron-rich intermetallic particles and partially soluble constituent particles were observed to be isolated and randomly distributed in the three orthogonal directions of the as-received plate. The final size of these intermetallic particles depends upon the fabrication procedure and ranges in size from 0.5 to 10 μm. Transmission electron microscopy observations revealed:

- Very well-defined grains of nonuniform size in the recrystallized regions (Fig. 3)
- The intermediate η′ precipitates dispersed in the alloy matrix (Fig. 4)
- Equilibrium η precipitates decorating the grain boundary regions (Fig. 5)

The tensile properties are summarized in Table 2. Details are discussed elsewhere (Ref 21).

4.2 *Tensile Deformation and Fracture Behavior*

The tensile fracture surfaces are helpful in elucidating microstructural effects on strength, ductility, deformation, and fracture properties of aluminum alloy 7055. Fractography of the tensile samples revealed that at a given test temperature, the macroscopic fracture morphology was essentially identical for both the longitudinal (L) and transverse (T) specimens. However, for each orientation, the fracture morphology was drastically different at the ambient and elevated temperatures. The difference is believed to be associated with different proportions of the fracture mode and the intrinsic features on the surface. Representative fracture features of the specimens are shown in Fig. 6-9.

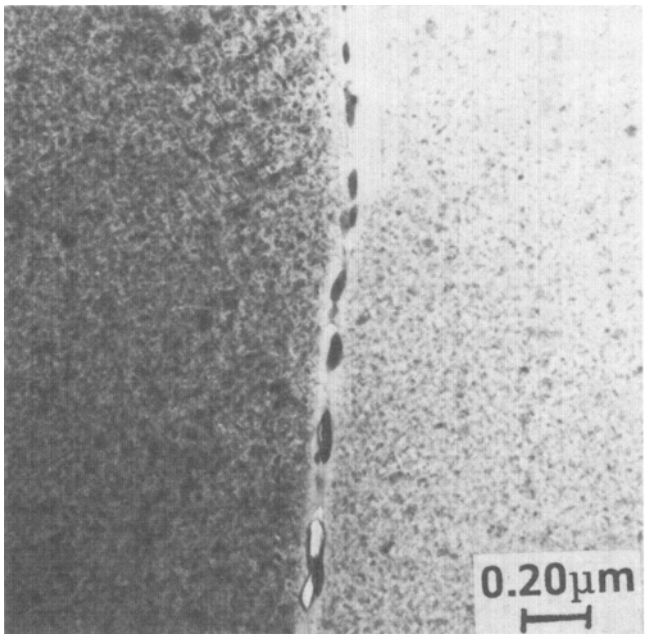

Fig. 5 Transmission electron micrograph showing the equilibrium η precipitates decorating the grain boundary and the narrow PFZ adjacent to the grain boundary region

4.2.1 Ambient Temperature (27 °C)

On a macroscopic scale, tensile fracture of the alloy was by shear, for both the longitudinal and transverse specimens, with the fracture surface oriented at approximately 40 to 45° to the major stress axis. The shear type of fracture tends to minimize necking and thus any triaxial state of stress and hydrostatic component that occurs in the necked region (Ref 22). Fracture was bimodal, comprising both transgranular and intergranular regions. Fracture of the deformed tensile samples revealed an overall macroscopically brittle appearance at low magnifications (Fig. 6a). At the microscopic level, samples revealed features reminiscent of both ductile failure, that is, voids of varying size and shallow dimples (Fig. 6c) and brittle failure, that is, cracking along the grain and subgrain boundaries (Fig. 6d). The shallow dimples are the end result of the presence of smaller second-phase particles, the zirconium dispersoids (β′: Al_3Zr) and the equilibrium grain boundary η precipitates. Since crack extension under quasi-static loading occurs at high stress intensities, comparable with the fracture toughness of the material, the presence of microscopic and macroscopic voids coupled with cracking along the grain and subgrain boundaries lowers the actual strain-to-failure associated with ductile fracture.

4.2.2 Test Temperature of 100 °C

At the elevated temperature of 100 °C, the macroscopic fracture mode, for both the longitudinal (L) and transverse (T) specimens, was at 45° to the far-field stress (load) axis following a plane of maximum macroscopic shear stress. High magnification observation revealed the transgranular regions to be covered with voids of a range of sizes and a bimodal distribution of dimples (Fig. 7a). The macroscopic voids were intermingled with fine microscopic voids. The applied far-field stress assists in the growth of these voids during the later stages of tensile deformation (Fig. 7b). The transgranular fracture regions were comprised of cracks along the grain boundaries parallel to the major stress axis (Fig. 7c) and were covered with isolated voids and shallow dimples (Fig. 7d). These dimples are the result of the presence of smaller insoluble phases (Al_2CuMg and Al_xCu_y), the equilibrium η precipitate, and the β′ dispersoids.

4.2.3 Test Temperature of 190 °C

At this temperature, the macroscopic fracture mode, for both the longitudinal and transverse specimens, was at 45° to the far-field stress axis following a plane of maximum macroscopic shear stress. The macroscopic fracture mode was ductile, while the microscopic fracture mode revealed features reminiscent of locally ductile mechanisms (Fig. 8). The fracture surface was covered with a large population of voids of varying size and shallow dimples. The macroscopic voids were intermingled with numerous fine microscopic voids. The voids and dimples were elongated in one direction, indicative of shearing dominated stresses prior to failure. Several of the macroscopic voids underwent substantial growth (Fig. 9). Cracking was not evident either along the grain or subgrain boundaries.

Table 2 Tensile properties of aluminum alloy 7055-T7751

Orientation	Temperature, °C	Elastic modulus, GPa	Yield strength MPa	Yield strength ksi	Tensile strength MPa	Tensile strength ksi	Elongation, %	Reduction in area, %	ln (A_0/A_f)(a), %
Longitudinal	27	70	610	90	630	92	12	16	16
	100	69	540	78	560	80	14	34	42
	190	65	395	57	400	58	23	40	44
Transverse	27	70	620	91	650	94	10	16	16
	100	66	570	82	575	83	14	31	37
	190	64	395	57	395	57	20	49	68

Results are mean values based on duplicate tests. Elastic modulus is tangency measurement based on extensometer trace. (a) A_0 = initial area of cross-section; A_f = final area of cross-section

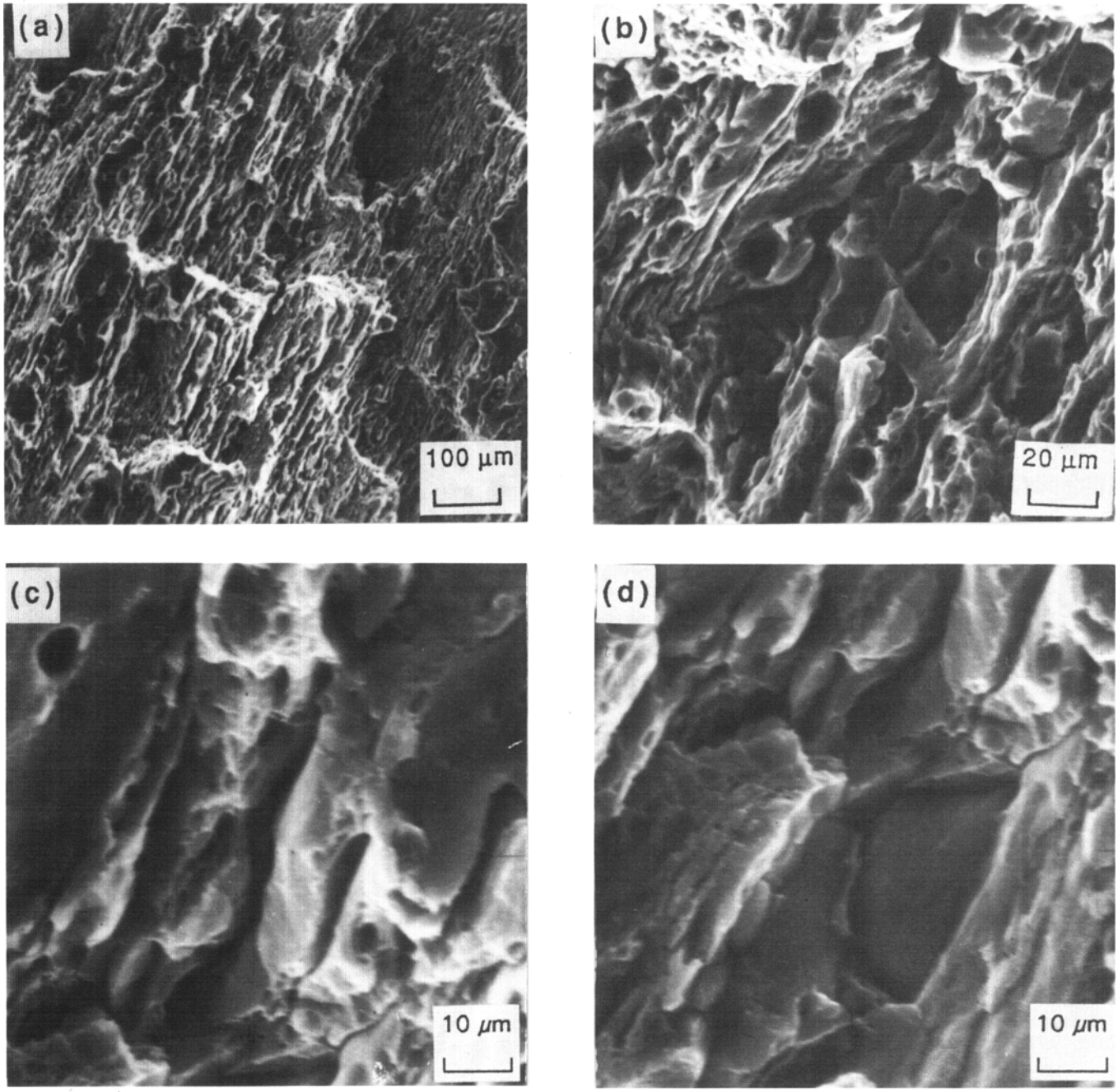

Fig. 6 Scanning electron micrographs of the tensile fracture surface of the longitudinal specimen deformed at 27 °C showing (a) overall morphology, (b) high magnification of (a), (c) voids and shallow dimples, and (d) cracking along the grain and subgrain boundaries

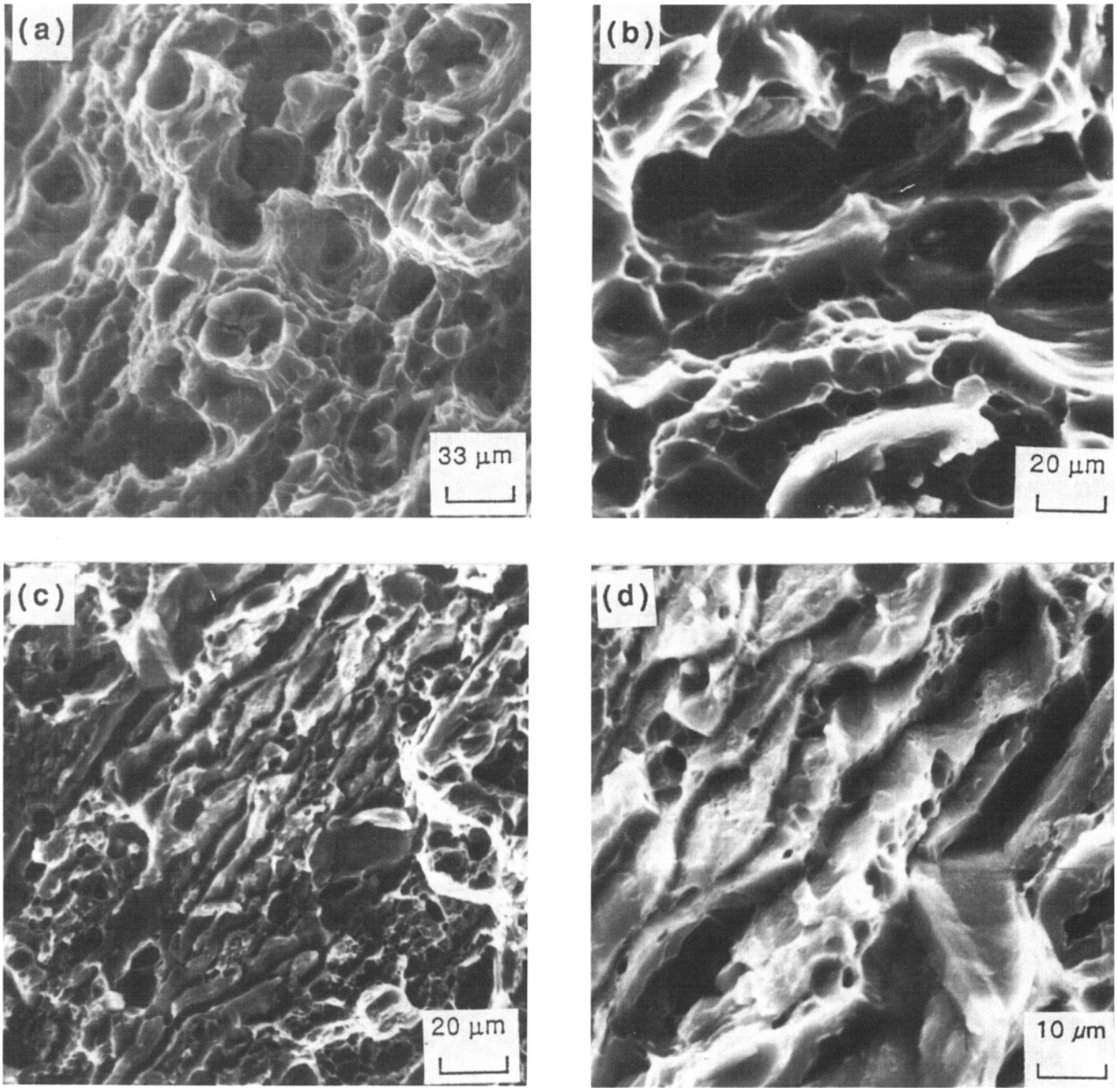

Fig. 7 Scanning electron micrographs of the tensile fracture surface of the longitudinal specimen deformed at 100 °C showing (a) overall morphology, (b) growth and coalescence of the microscopic voids, (c) cracking along the high angle grain boundaries, and (d) high magnification of (b) showing distribution of voids and shallow dimples

5. Discussion

The micromechanisms governing the deformation and fracture characteristics of this alloy in the T7751 microstructural condition are dictated by intrinsic microstructural features such as (a) the nature (degree of coherency) and distribution of the primary strengthening precipitates, (b) distribution of the coarse and intermediate size intermetallic particles, (c) nature of grain boundary precipitates and particles, (d) volume fraction of second-phase particles, (e) degree of ordering, and (f) texture. Consideration of the strengthening mechanism of the alloy is essential because it markedly influences the deformation and final fracture processes.

During uniaxial straining, the tendency toward localized inhomogeneous deformation due to repeated shearing of the strengthening η' precipitates dispersed in the alloy matrix results in a local decrease in resistance to dislocation motion and a concentration of slip in narrow bands through the grain. The slip concentration causes localization of strain at the grain

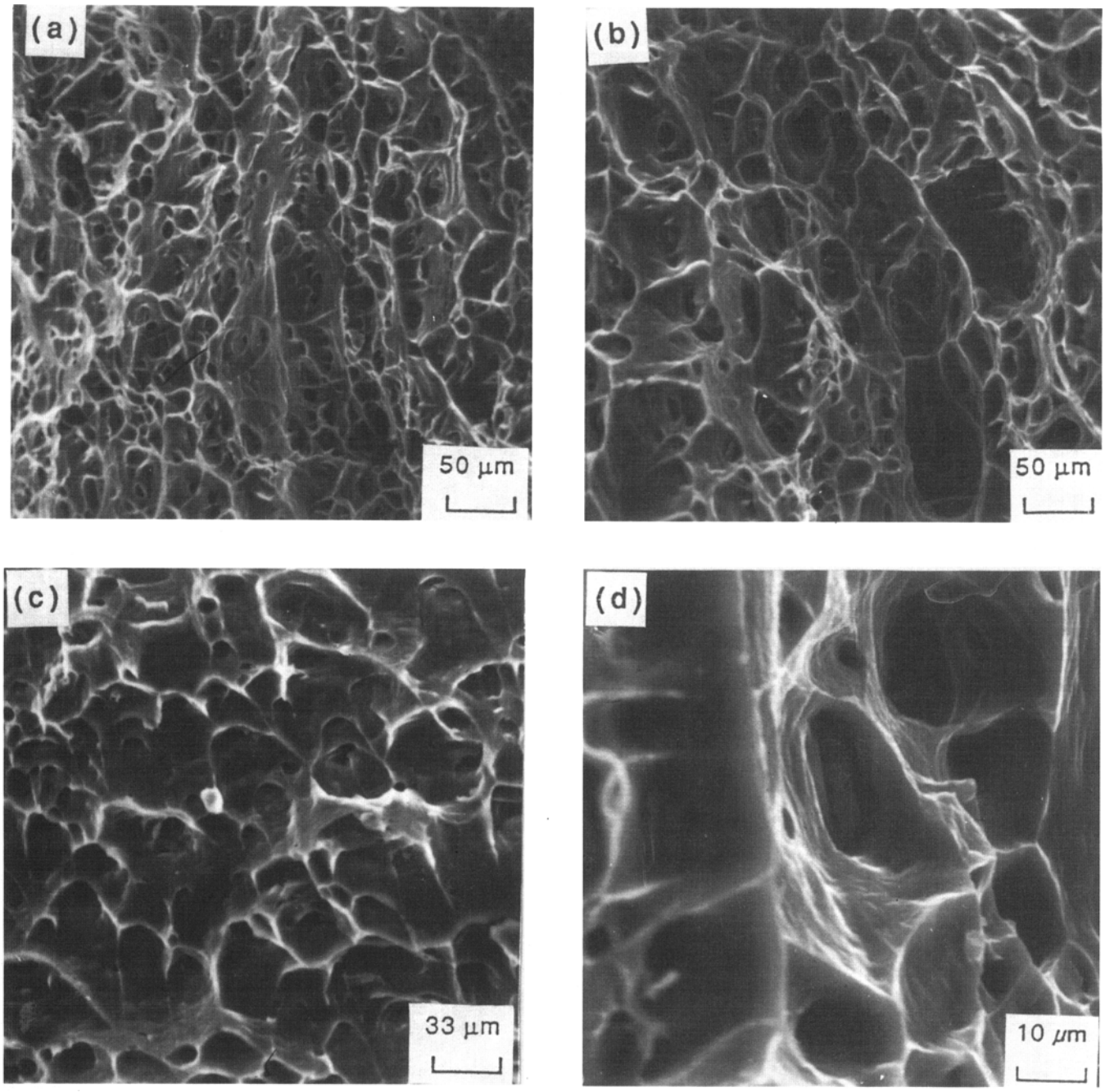

Fig. 8 Scanning electron micrographs of the tensile fracture surface of the longitudinal specimen deformed at 190 °C

boundary regions. In fact, occurrence of transcrystalline localization is favored by the conjoint and mutually interactive influences of a high level of critical resolved shear stress and shearable precipitate particles. Repeated shearing of these particles leads to a progressive reduction of their size and a concomitant reduction in the overall resistance to the motion of dislocations. The number of dislocations that pass on a typical plane from the initiation of deformation until local slip ends can be used as an indicator of slip localization (Ref 23). The planar slip bands (Fig. 10), resulting from the interaction of the slip dislocations with the precipitate particles, impinge upon the grain and subgrain boundaries and cause a shear stress concentration at the point of impingement on the boundary. Mott (Ref 24) suggested that the stress concentration (τ^*) around the piled-up dislocations at the end of the slip band may be adequate enough to initiate a crack. When τ^* exceeds the crack nucleation stress at the grain boundary regions, microcrack initiation and intergranular fracture are favored (Fig. 11) (Ref 23, 25, 26). This is aided by the presence of grain boundary precipitates and particles and narrow precipitate-free zones (PFZs), which favor concentration of deformation and concomitant microcrack initiation at these regions. In the presence of PFZs, adjacent to the grain boundary regions, plastic relaxation is favored within these soft zones. The extent of plastic re-

laxation is dependent on the width of the PFZ. The long-range stresses caused by the pile-up of dislocations on the blocked slip band produce tensile stresses that equal or exceed the cohesive strength of the grain boundary. As a result, low energy grain boundary or intergranular fracture is favored. This is exacerbated by the presence of grain boundary particles and precipitates. Since the PFZs are considerably weaker than the matrix ($\sigma_{PFZ} << \sigma_{matrix}$), they are potential sites for preferential plastic deformation resulting in high local stress concentration at grain boundary triple junctions. Once the cracks nucleate, either at the grain boundary or at grain boundary particles, they propagate intergranularly within the soft PFZ.

Initiation of voids is favored at the intersection of an inhomogeneous planar deformation band and a grain boundary particle or precipitate (Fig. 12). The applied far-field stress assists in the growth of these voids. The fine microscopic voids coalesce, and the halves of these voids are the shallow dimples found adjacent to the intergranular fracture regions (Fig. 13).

Void initiation at the coarse and intermediate size intermetallic and constituent particles is governed by the conjoint influence of inclusion size, stress and local strain levels, and matrix deformation characteristics. The iron-rich intermetallics and insoluble constituent particles, coupled with a matrix microstructure that favors localized inhomogeneous deformation, facilitates the nucleation and coalescence of voids to occur at low to moderate stress levels. In fact, void nucleation at a coarse second-phase particle occurs when the elastic energy in the par-

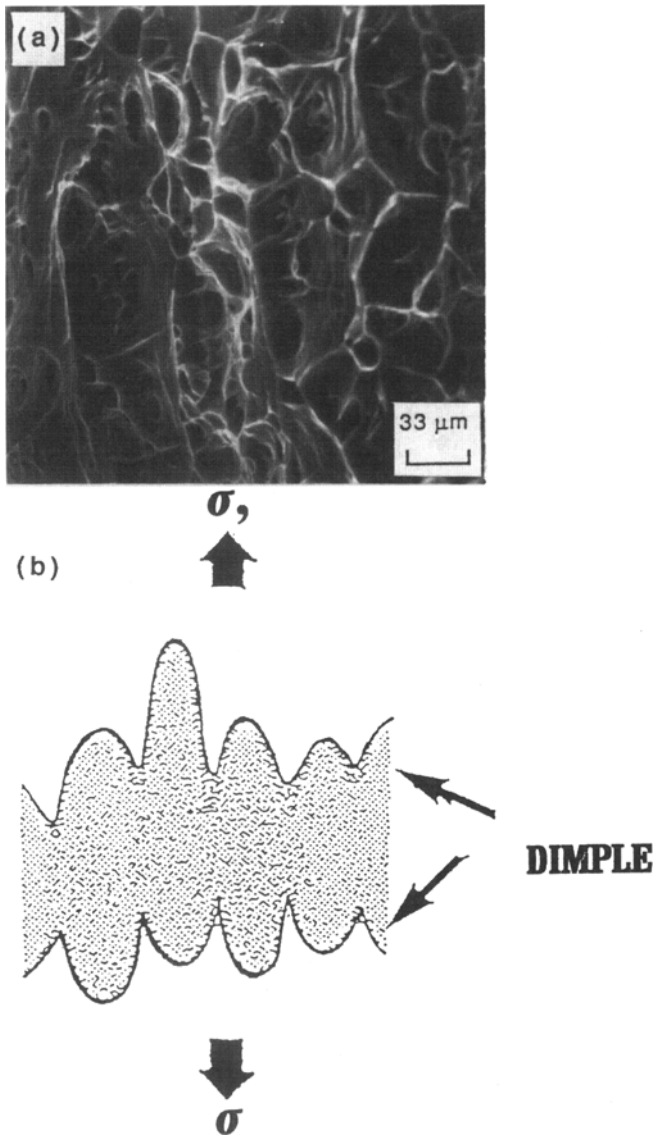

Fig. 9 (a) Scanning electron micrograph showing dimples on the tensile fracture surface of aluminum alloy 7055. (b) Schematic representation of dimple formation

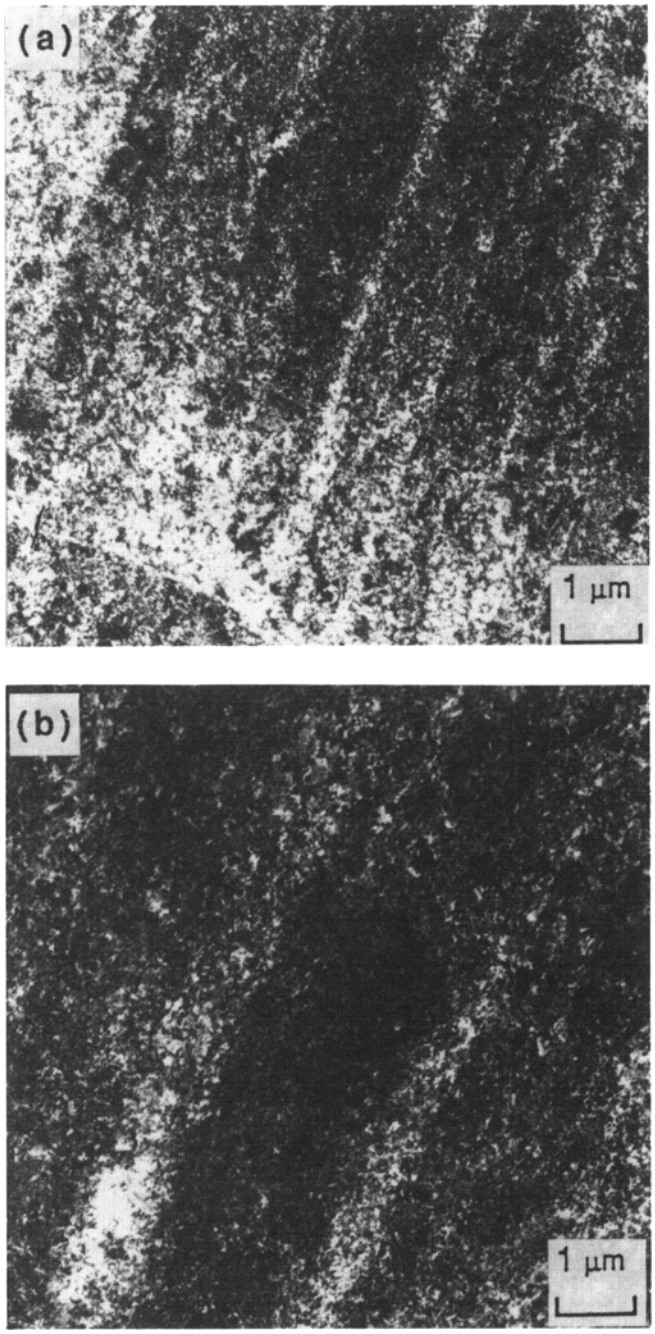

Fig. 10 Bright field TEM showing planar deformation bands in aluminum alloy 7055-T7751. (a) 27 °C. (b) 100 °C

ticle exceeds the surface energy of the newly formed void surfaces (Ref 27, 28). While satisfying this energy criterion is a necessary condition, it must also be aided by a stress on the matrix-particle interfaces in excess of the interfacial strength (Ref 29, 30). When stress buildup at the particle-matrix interfaces reaches a critical value, void nucleation occurs by interface separation. For the 7055 aluminum alloy in the microstructural condition studied, the interface stress consists of the applied far-field stress (σ_A) and the normal stress due to blocked slip bands (σ_P) (Ref 31). When a critical value of stress is reached, void nucleation occurs provided sufficient elastic energy is available for the creation of new void surfaces.

Coalescence of the macroscopic voids is aided by the fine microscopic voids. During the coalescence stage, void-void interactions occur during the period when void growth is accelerated. The macroscopic voids are created by fracture of the coarse intermetallic particles and constituent phases, and they coalesce by impingement, that is, the voids grow until they

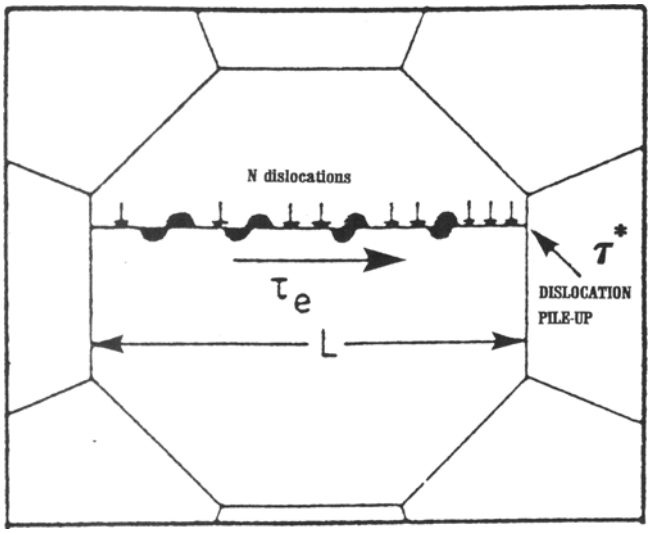

Fig. 11 Schematic showing shear stress (τ_e) and shear stress concentration (τ^*) in a dislocation pileup

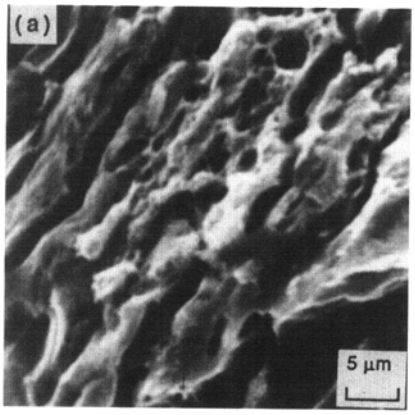

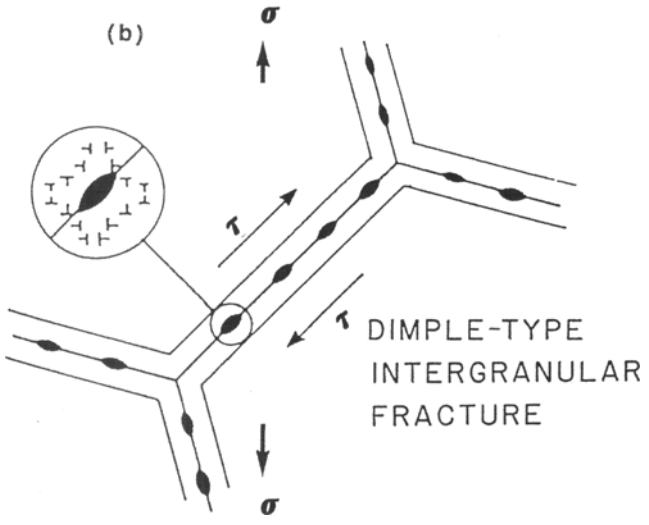

Fig. 13 (a) Scanning electron micrograph showing voids and dimples adjacent to the intergranular fracture regions. (b) Schematic showing dimple-formation type intergranular fracture

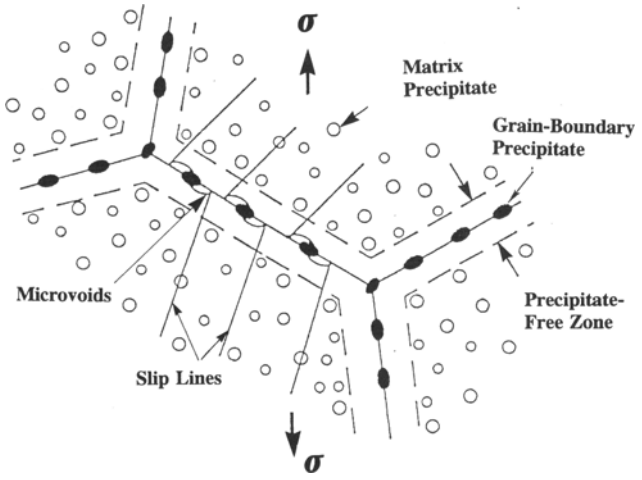

Fig. 12 Schematic showing the deformation process in the presence of narrow PFZ and grain boundary precipitates

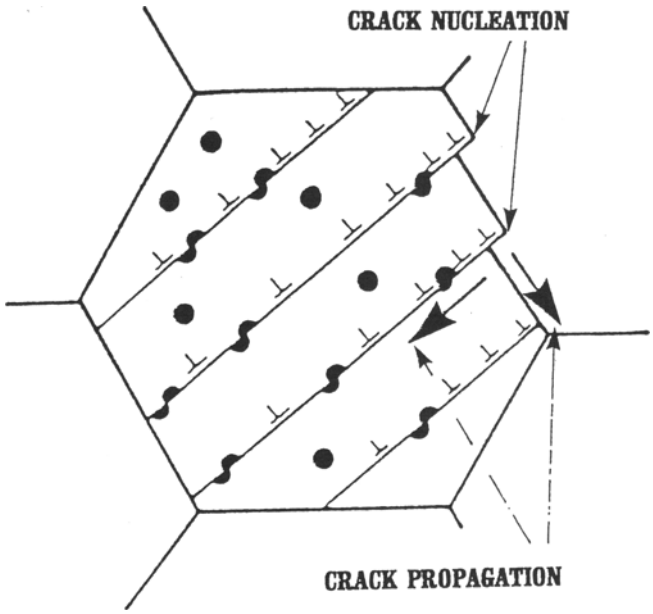

Fig. 14 Schematic illustration of the deformation and quasi-static fracture sequence in aluminum alloy 7055-T7751

touch each other. However, the more widely separated macroscopic voids coalesce by linking of the microscopic voids to form void sheets. The coalescence of fine microscopic voids initiated at the grain boundary precipitates and particles results in a dimple-formation type intergranular fracture (Fig. 13). The tensile deformation and fracture sequence occurring in aluminum alloy 7055-T7751 is succinctly summarized in Fig. 14.

6. Conclusions

The overall conclusions of this investigation on the quasi-static fracture characteristics of aluminum alloy 7055 are:

- The alloy has a partially recrystallized microstructure with the large recrystallized grains flattened and elongated in the longitudinal direction. The insoluble intermetallic particles and partially soluble constituent phases were observed to be isolated and randomly distributed along the three orthogonal directions of the rolled plate.
- The strength of the alloy decreased with an increase in test temperature. The ductility, quantified in terms of tensile elongation and reduction in area, showed a significant increase with test temperature.
- Tensile deformation structures revealed the predominant mode to be inhomogeneous with the formation of planar slip bands. The slip bands were intense at the elevated temperature.
- At a given test temperature, macroscopic fracture was essentially similar for both the longitudinal and transverse specimens. Macroscopic fracture of the alloy was predominantly by shear, while microscopic fracture revealed features reminiscent of both brittle and locally ductile mechanisms, that is, combination of intergranular and intersubgranular cracking coupled with ductile microvoid formation, growth, and coalescence.

Acknowledgments

The authors gratefully acknowledge the support of The University of Akron (Faculty Research Grant 2-07299) and the Aluminum Company of America (Program Managers: Drs. J. Liu and Gary H. Bray) for providing the material used in this study.

References

1. J.G. Kaufman, "Design of Aluminum Alloys for High Toughness and High Fatigue Strength," 40th Meeting of Structures and Materials Panel, (Brussels, Belgium), NATO, April 1975
2. R.E. Sanders, Jr. and E.A. Starke, Jr., *Metall. Trans. A*, Vol 6, 1978, p 1087
3. M.V. Hyatt and W.E. Quist, AFML Technical Report, TR-67-329, 1967
4. E.A. Starke, Jr. and W.E. Quist, in *Flight Vehicle Materials, Structures and Dynamics: Assessment and Future Directions*, Vol 2, A.K. Noor and S.L. Venneri, Ed., American Society of Mechanical Engineers, 1992, p 118-160
5. J.T. Staley, Technical Report, Contract M00019-71-C-0131, Naval Air Systems Command, May 1972
6. J.T. Staley, "Microstructure and Toughness of High Strength Aluminum Alloys," presented at ASTM Symposium on Properties as Related to Toughness, (Montreal, Canada), ASTM, June 1975
7. J.S. Santner, AFML Technical Report, TR-76-200, March 1977
8. F. Ostermann, *Metall. Trans.*, Vol 2, 1971, p 2897-2902
9. E. DiRusso, M. Conserva, F. Gatto, and H. Markus, *Metall. Trans.*, Vol 4, 1973, p 1133-1144
10. W.H. Reimann and A.W. Brisbane, *Eng. Fract. Mech.*, Vol 5, 1973, p 67-78
11. D.S. Thompson, S.A. Levy, and D.K. Benson, Thermomechanical Aging of Aluminum Alloys, *Third International Conference on Strength of Metals and Alloys*, Cambridge University Press, England, 1973, p 119-123
12. J.E. Vruggink, Technical Report, 76073, Frankford-Arsenal, April 1977
13. H. Sulinski and J. Waldman, Summary Report, Frankford-Arsenal, July 1976
14. J.T. Staley and R.L. Rolf, International Symposium on Light Metals, The Minerals, Metals and Materials Society, August 1993
15. J.T. Staley, Aluminum Alloys and Composites, *Encyclopedia of Physical Science*, Elsevier Applied Science, NY, Vol 1, 1992, p 591-598
16. E.A. Starke, Jr., *Mater. Sci. Eng.*, Vol 29, 1977, p 99-112
17. E. Hornbogen and E.A. Starke, Jr., *Acta Metall. Mater.*, Vol 41 (No. 1), 1993, p 1-16
18. L.F. Mondolfo, N.A. Gjoestein, and P.W. Levinson, *Trans. AIME*, Vol 206, 1956, p 1311
19. J.T. Staley, *Metall. Trans. A*, Vol 5, 1974, p 929-940
20. "Tension Testing of Metallic Materials," E-8-93, ASTM, 1993
21. S. Anand, "The Cyclic Fatigue and Fracture Behavior of Two High Strength Al-Zn-Mg-Cu Alloys," Master of Science thesis, University of Akron, 1992
22. R.E. Crooks and E.A. Starke, Jr., *Metall. Trans. A*, Vol 15, 1984, p 1367
23. J.P. Hirth and J. Lothe, *Theory of Dislocations*, McGraw Hill, 1968, p 694
24. N.F. Mott, *Proc. R. Soc. A*, Vol 200, 1953, p 1
25. A.H. Stroh, *Proc. R. Soc. A*, Vol 223, 1954, p 404
26. J.M. Duva, M.A. Daubler, E.A. Starke, Jr., and G. Lutjering, *Acta Metall.*, Vol 36, 1988, p 585
27. J. Gurland and J. Plateau, *Trans. ASM*, Vol 56, 1963, p 442
28. R.H. Van Stone and J.A. Psioda, *Metall. Trans. A*, Vol 6, 1975, p 672
29. A.S. Argon, J. Im, and A. Needleman, *Metall. Trans. A*, Vol 6, 1975, p 825
30. A.S. Argon, *J. Eng. Mater. Technol.*, Vol 98, 1976, p 60